Please provide feedback

Please support the ScholarWorks@UMBC repository by emailing scholarworks-group@umbc.edu and telling us what having access to this work means to you and why it's important to you. Thank you.

Phase space structure of the electron diffusion region in reconnection with weak guide fields

J. Ng, J. Egedal, A. Le, and W. Daughton

View Online   Export Citation   CrossMark

ARTICLES YOU MAY BE INTERESTED IN

A review of pressure anisotropy caused by electron trapping in collisionless plasma, and its implications for magnetic reconnection
Physics of Plasmas **20**, 061201 (2013); https://doi.org/10.1063/1.4811092

The mechanisms of electron heating and acceleration during magnetic reconnection
Physics of Plasmas **21**, 092304 (2014); https://doi.org/10.1063/1.4894484

The diffusion region in collisionless magnetic reconnection
Physics of Plasmas **6**, 1781 (1999); https://doi.org/10.1063/1.873436

Physics of Plasmas
Features in **Plasma Physics Webinars**

Register Today!

Phase space structure of the electron diffusion region in reconnection with weak guide fields

J. Ng,[1] J. Egedal,[1,a)] A. Le,[1] and W. Daughton[2]

[1]*Department of Physics, and Plasma Science and Fusion Center, Massachusetts Institute of Technology, Cambridge, Massachusetts 02139, USA*
[2]*Los Alamos National Laboratory, Los Alamos, New Mexico 87545, USA*

Kinetic simulations of magnetic reconnection provide detailed information about the electric and magnetic structure throughout the simulation domain, as well as high resolution profiles of the essential fluid parameters including the electron and ion densities, flows, and pressure tensors. However, the electron distribution function, $f(v)$, within the electron diffusion region becomes highly structured in the three dimensional velocity space and is not well resolved by the data available from the particle-in-cell (PIC) simulations. Here, we reconstruct the electron distribution function within the diffusion region at enhanced resolution. This is achieved by tracing electron orbits in the fields taken from PIC simulations back to the inflow region where an analytic form of the magnetized electron distribution is known. For antiparallel reconnection, the analysis reveals the highly structured nature of $f(v)$, with striations corresponding to the number of times electrons have been reflected within the reconnection current layer, and exposes the origin of gradients in the electron pressure tensor important for momentum balance. The structure of the reconnection region is strongly tied to the pressure anisotropy that develops in the electrons upstream of the reconnection region. The addition of a guide field changes the nature of the electron distributions, and the differences are accounted for by studying the motion of single particles in the field geometry. Finally, the geometry of small guide field reconnection is shown to be highly sensitive to the ion/electron mass ratio applied in the simulation. © *2012 American Institute of Physics*. [http://dx.doi.org/10.1063/1.4766895]

I. INTRODUCTION

Magnetic reconnection is a change in topology of the magnetic field lines in a plasma,[1] often with the conversion of stored magnetic energy to the kinetic energy of accelerated particles. It is believed to play a vital role in a variety of laboratory and astrophysical plasma processes, including solar flares, magnetic substorms in the Earth's magnetosphere, and coronal mass ejections.[2–5]

In collisionless reconnection, the electron diffusion region, where the electron motion decouples from the magnetic field lines, is an area of significant interest. While a large body of work shows that the rate of reconnection is independent of the exact mechanism that allows the electron fluid to decouple from the magnetic field,[6] an understanding of the structure of the inner reconnection region may hold the key to determine how and under what conditions fast reconnection is initiated. Fully kinetic particle-in-cell (PIC) simulations have yielded a wealth of information on the structure of the reconnection region. In addition, spacecraft missions have provided *in situ* measurements of the electron distribution in the vicinity of the reconnection region. However, PIC simulations are often too noisy for determining the fine structure of the 7D electron distributions function $f(t, \mathbf{x}, \mathbf{v})$ and spacecraft observations still lack the high time resolution required to resolve the structures in f during short lasting encounters with reconnection regions in, say, the

Earth's magnetosphere.[7,8] Emphasizing the importance attributed to the electron physics within the reconnection region, NASA's Magnetospheric-Multiscale (MMS) mission is underway where four spacecraft, optimized for measuring the details of the electron distributions during reconnection, will be deployed in the Earth's magnetotail.

Recently, for anti-parallel reconnection, the structure of the electron distribution within the reconnection region in a PIC simulation has been obtained at unprecedented high resolution, revealing its structured nature.[9] This was accomplished using Liouville's theorem ($df/dt = 0$ along particle orbits) in the field geometry of a kinetic simulation, following the orbits of electrons backward in time until they reached the inflow where an analytic form of the electron distribution is known[10,11] and can be used as an upstream boundary condition. The strong anisotropy that develops in the inflow region and is accounted for in the analytic form explains the formation of the elongated electron jets observed in simulations of antiparallel reconnection.[12,13] In addition, it was shown how the anisotropy is important in determining the structure of the electron distribution in the diffusion region.[9]

In this paper, the orbit tracing method of Ref. 9 is applied to simulations of reconnection with small guide fields, a more generic regime relevant to nature. This reveals highly structured and complicated electron distributions governed by the dynamics of the electrons in the region in conjunction with the anisotropic electron pressure that develops upstream in the reconnection inflow region. In addition, as it

a)jegedal@psfc.mit.edu.

has been shown that the reconnection geometry is sensitive to the mass ratio used in the simulations,[14] both reduced and full mass ratio simulations are studied and the electron distributions compared.

This paper is organized as follows: in Sec. II, the orbit tracing method used to reconstruct the electron distribution is reviewed. In Sec. III, the structure of the electron distribution in the diffusion region in antiparallel reconnection is reconstructed, and the distributions obtained validated against the simulation data. In Sec. IV, the method is applied to data from simulations with small guide fields, and a similar scan is performed at full mass ratio. Finally, in Sec, V, the paper is summarized and concluded.

II. ORBIT TRACING METHOD

In order to study the internal structure of the electron diffusion region in detail, simulations from the fully kinetic particle-in-cell code VPIC[15] are used in conjunction with the tracing of electron trajectories. The electron distribution is reconstructed at high resolution through the use of Liouville's theorem. Starting at a point within the diffusion region, the equations of motion for electrons with different initial velocities are integrated backwards in time numerically using the

electric and magnetic fields from a single time slice of the PIC simulation.

Once the electrons reach the inflow region where $f(v_\parallel, v_\perp)$ is known, the value of $f(\mathbf{x}, \mathbf{v})$ is obtained directly. For this inflow distribution $f(v_\parallel, v_\perp)$, we use the analytic form given in the Appendix, which is the relativistic generalization of the theoretical distribution derived in Ref. 10. The analytic inflow distribution includes the effect of electrons becoming trapped in magnetic wells and by parallel electric fields; its form is characterized by the ratio between the magnetic field and the asymptotic magnetic field B/B_∞ and acceleration potential $\Phi_\parallel$. The anisotropic distribution at a point just upstream of the electron diffusion region is shown in Fig. 1(e). At this point, the trapped electrons make up the bulk of the distribution. Because the magnetic moments of the individual electrons are conserved, the perpendicular temperature of the trapped population is approximately $T_e B/B_\infty$ and it follows that $f(v_\parallel, v_\perp)$ is only large if $\frac{1}{2}mv_\perp^2 \leq T_e B/B_\infty$ and $\frac{1}{2}mv_\parallel^2 \leq e\Phi_\parallel$, where $T_e B/B_\infty \ll e\Phi_\parallel$. Given that the analytic form of the distribution in the inflow is known, the role of $\Phi_\parallel$ and B/B_∞ to the structure of the distribution in the diffusion can be tested by manipulating their values, which will be shown in the following section.
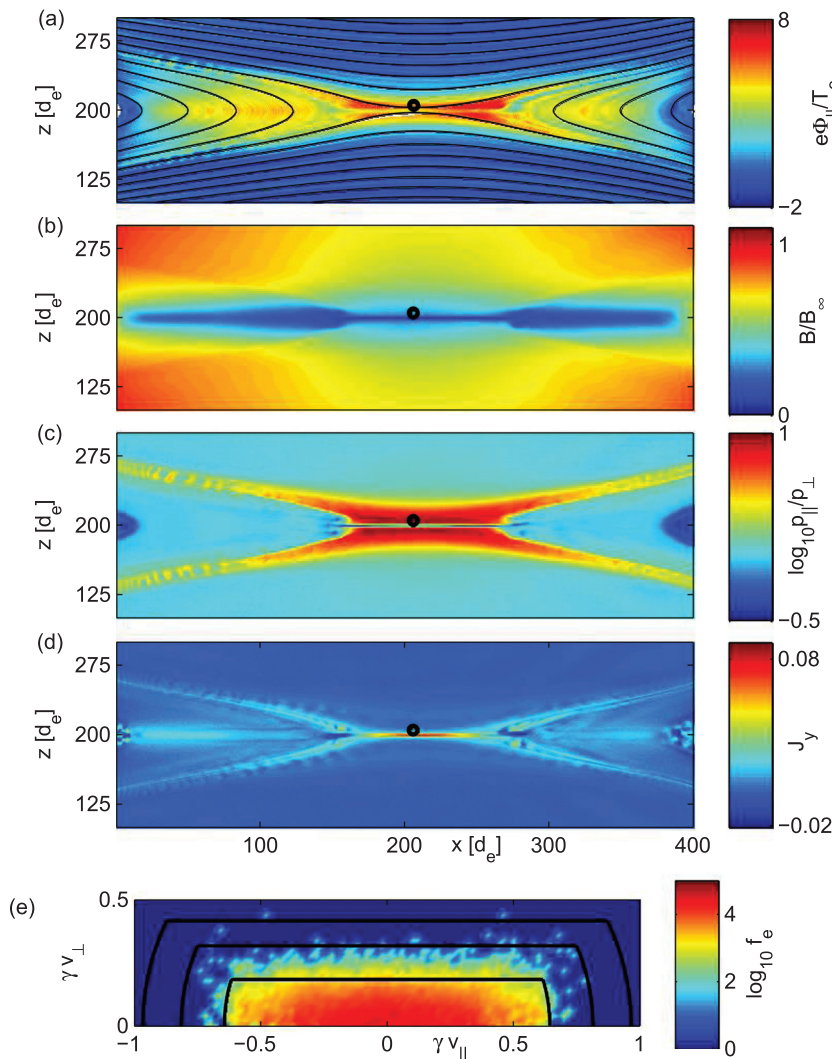

FIG. 1. Time slice from an open-boundary PIC simulation of anti-parallel reconnection. (a) Acceleration potential $e\Phi_\parallel/T_e$. (b) Magnetic field strength B. (c) Pressure anisotropy $\log_{10}(p_\parallel/p_\perp)$. (d) Out of plane current density J_y (normalized to en_0c). (e) Distribution function just upstream of the electron diffusion region at the point marked with circles. The color plot shows data from the PIC code, while the black contour lines are from the analytic form of f in Appendix.

All the simulations applied are translationally symmetric in the y direction and have domains of $20d_i \times 20d_i$. The initial state is a Harris sheet[16] characterized by $T_i/T_e = 5$, $v_{the}/c = 0.13$, $\omega_{pe}/\omega_{ce} = 2$, and a background plasma with density $= 0.23n_0$, where n_0 is the peak Harris density. Simulations are performed at mass ratios $m_i/m_e = 400$ and 1836, keeping the size of the simulation domain in d_i fixed. The code tracks roughly 2×10^9 to 2×10^{10} particles and as described in Ref. 12, at all domain boundaries open boundary conditions are applied for the particles and fields. Magnetic reconnection develops from a small initial perturbation. The coordinate system is defined with the x axis along the outflow direction, z axis along the inflow, and y axis into the page. Unless otherwise mentioned, distances are measured in terms of d_e, while velocities are given in terms of c.

III. ANTIPARALLEL RECONNECTION

We start by providing a more in-depth analysis of the antiparallel ($B_g = 0$) reconnection geometry at mass ratio 400

studied in Ref. 9. The simulation domain is 2560×2560 cells $= 400d_e \times 400d_e$, where $d_e = c/\omega_{pe}$ is the electron inertial skin depth. In Fig. 1, $\Phi_\parallel$, B, $\log_{10}(p_\parallel/p_\perp)$ and J_y at time $t\Omega_{ci} = 19$ are shown, after reconnection has reached a near steady state. Close to the layer, $e\Phi_\parallel/T_e$ reaches a maximum value of approximately 7 while the ratio $p_\parallel/p_\perp$ is about 9.

Using the orbit tracing method described in the preceding section, the electron distributions from points on a cut along the z-axis close to the x-line are obtained. These are shown in Fig. 2(a), where the coloured plots show the averaged values over v_x, v_y, and v_z, respectively. Within the layer, the distribution is highly structured, and a phase space hole in v_z is observed,[17] splitting the distribution into two somewhat triangular portions which extend to large values of v_y. This hole is caused by the electron meandering motion in the diffusion region and the inversion layer of the in-plane electric field E_z (see Ref. 18). Due to the width of the distribution in the v_x direction, the contributions of the large $|v_y|$ electrons are washed out in the v_y-v_z plots. Also observed are a number of striations, most noticeable in the v_x-v_y plane.
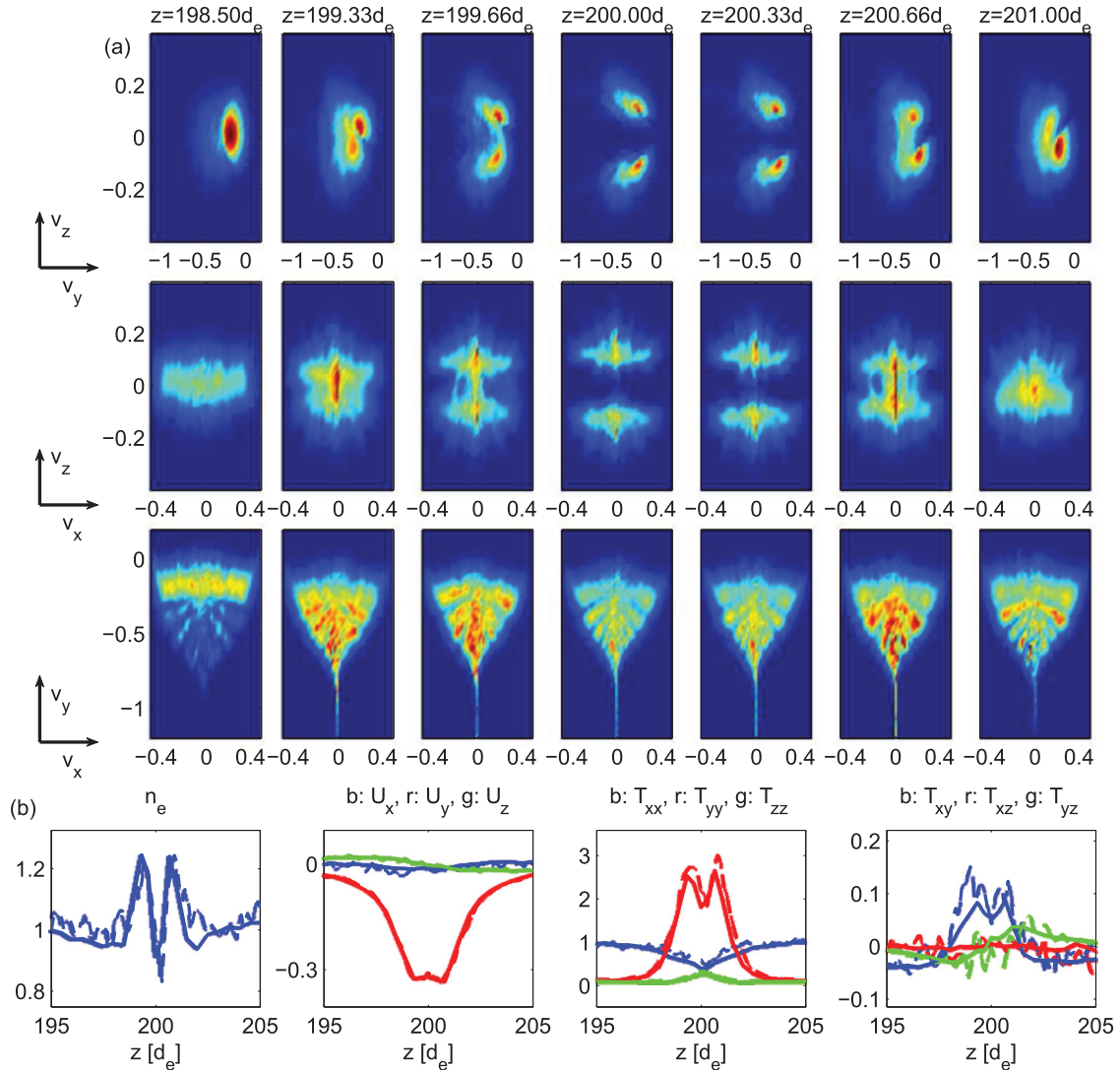

FIG. 2. Plots of reconstructed distribution function along a cut at $x = 206.25d_e$. Velocity units are in terms of c. (a) Distribution function averaged over γv_x, γv_y, and γv_z, where γ is the Lorentz factor. (b) Moments of the electron distribution for a cut along the z axis passing through the x-line. From left to right, the density, fluid velocity, diagonal, and off-diagonal components of the pressure tensor are plotted. The dashed lines show the data from the PIC simulation while the solid lines show the reconstructed moments. Density and pressure components are normalized to n_0 and the value of $T_{xx} = m_e \int v_x v_x f d^3 v/\gamma$ outside the layer.

Moving outside the layer, the separation in v_z and extension in v_y decrease, eventually becoming the elongated distribution characteristic of the inflow region.

Taking moments of the reconstructed distribution, the density, fluid velocity, and pressure tensor can be obtained and compared with the data taken directly from the PIC code in order to verify the validity of the reconstructed f. As shown in Fig. 2(b), good agreement is found between both sets of data. This provides evidence of the accuracy of the reconstructed distributions.

A more detailed three-dimensional view of the reconstructed distribution function at locations around the x-line is shown in Figs. 3(a) and 4(a)–4(d). As mentioned earlier, the two main portions of the distribution ($v_z < 0$ and $v_z > 0$) are further divided by numerous striations. Tracing of orbits reveals that the striations are characterized by the number of times electrons are reflected in the z-direction within the layer before reaching the point of interest, with larger $|v_y|$ corresponding to a larger number of reflections. These oscillations are the characteristic of meandering electron motion in a field reversal.[19]

In the layer, the electric and magnetic fields are well approximated by

$$\mathbf{E} = E_y\hat{\mathbf{y}}, \quad \mathbf{B} = B_0\left(\frac{z}{d}\hat{\mathbf{x}} + \frac{x}{L}\hat{\mathbf{z}}\right). \quad (1)$$

Here, d and L are typical length scales of the thickness and width of the electron diffusion region, with $d \sim d_e$ and $L \gg d$. As such, the equations of motion can be written as

$$\ddot{x} = -\frac{e}{m_e}\left(\dot{y}B_0\frac{x}{L}\right),$$
$$\ddot{y} = -\frac{e}{m_e}\left(E_y + \dot{z}B_0\frac{z}{d} - \dot{x}B_0\frac{x}{L}\right), \quad (2)$$
$$\ddot{z} = -\frac{e}{m_e}\left(-\dot{y}B_0\frac{z}{d}\right).$$

If the E_y term in the y equation is assumed to dominate, the x and z equations of motion reduce to

$$\ddot{x} = -\frac{e}{m_e}\left(\left(\dot{y}_0 - \frac{e}{m_e}E_yt\right)B_0\frac{x}{L}\right)$$
$$\ddot{z} = -\frac{e}{m_e}\left(-\left(\dot{y}_0 - \frac{e}{m_e}E_yt\right)B_0\frac{z}{d}\right), \quad (3)$$

whose solutions are linear combinations of Airy functions.[19,20] This accounts for the oscillatory motion in the z direction and eventual ejection of the electrons in the x direction. Typical trajectories with 0, 1, and 2 reflections are shown in Fig. 3(b). This classification by the number of reflections is also seen in Refs. 21 and 22, though they do not capture the full three dimensional structure of the electron distribution.

To explain the form of the striations, it is important to note the anisotropic form of the distribution in the inflow just upstream of the layer, shown in Fig. 1(e). The regions with large f in the reconstructed distribution mainly correspond to trapped particles in the inflow distribution, and we can thus obtain the center of the striations by injecting electrons
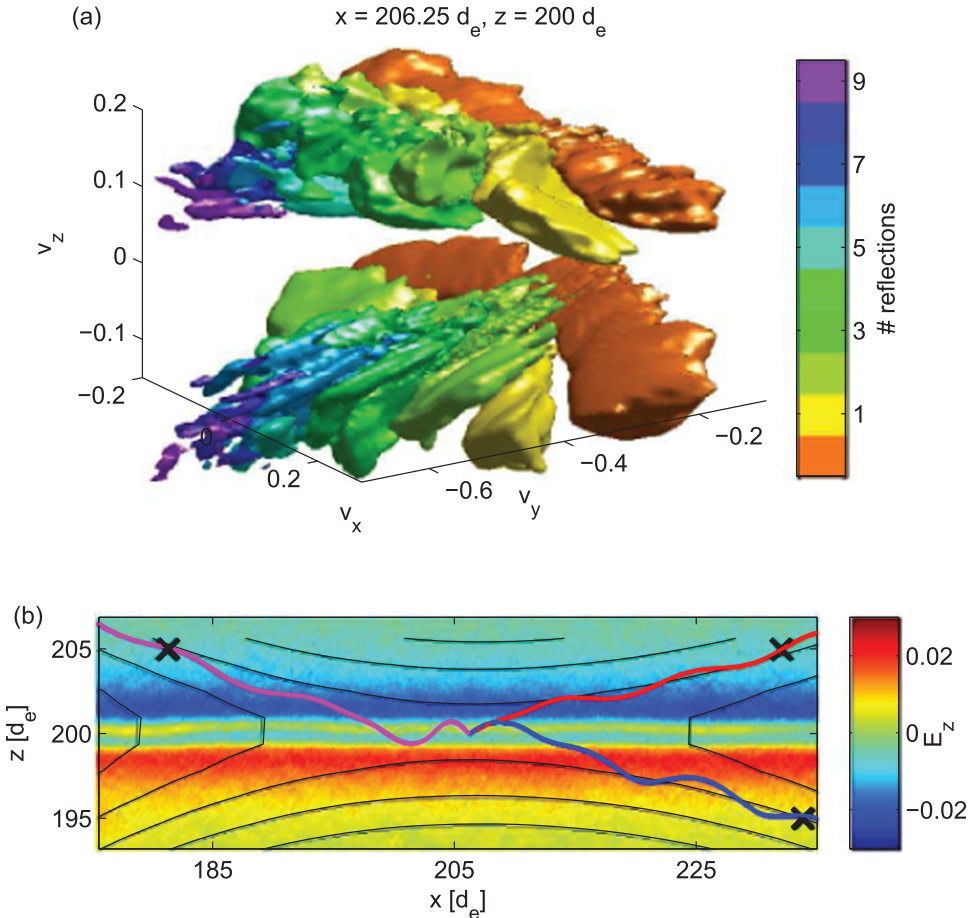

FIG. 3. Electron distribution within neutral sheet. (a) Isosurface of the distribution at x-line. The different colors correspond to the number of times the electrons are reflected in the layer. (b) Electron orbits from x-line with 0, 1, and 2 reflections. Color plot is in-plane electric field E_z, with contours of in-plane projection of magnetic field lines.
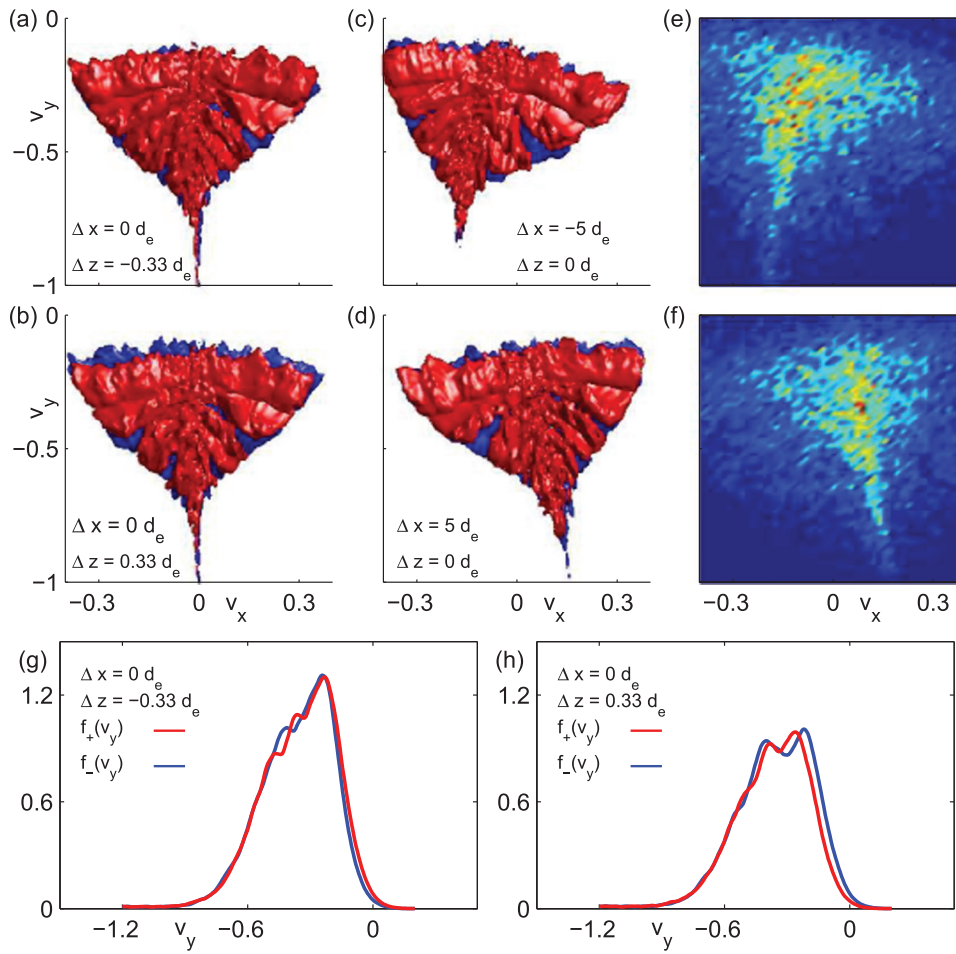
FIG. 4. (a) and (b) Isosurfaces of the distribution at $\Delta z = \pm 0.33 d_e$ above and below x-line at $(x, z) = (206.25, 200)$. The red region lies in $v_z > 0$, the blue in $v_z < 0$. Note the relative displacement in v_y of the red and blue surfaces as z increases, causing a gradient in P_{yz}. (c) and (d) Isosurfaces of the distribution at $\Delta x = \pm 5 d_e$ to the left and right of the x-line. Rotation of the distribution along the layer causes the gradient in P_{xy}. (e) and (f) v_x-v_y distribution of particles taken from PIC simulation at $\Delta x = \pm 5 d_e$. (g) and (h) The distributions in (a), (b) after integrating over v_x and v_z, showing the $v_z < 0$ and $v_z > 0$ contributions separately (making the displacement in v_y clearer). Vertical axis units are arbitrary. The red line represents $v_z > 0$, while the blue is for $v_z < 0$.

parallel to the outside magnetic field ($v_\perp = 0$), with $\frac{1}{2}mv_\parallel^2 \leq e\Phi_\parallel$. As the tip of each striation consists of the highest energy electrons, their lengths are approximately determined by the acceleration potential $\Phi_\parallel$.

To further validate the result, particle data taken directly from the PIC simulation are presented in Figs. 4(e) and 4(f). This confirms the general form of the reconstructed distribution, and illustrates a key advantage of the orbit tracing method, as the resolution achieved spatially and in and velocity space is much higher due to the ability to select as many velocity points as necessary (here 200^3 are used).

The different parts of the distribution correspond to electrons originating from the four quadrants in the x-z plane. By considering their trajectories, it is clear that those with positive v_x originated from the left of the x-line, and those with negative v_x from the right. The entry z position is determined by the number of reflections and the sign of v_z. For example, the trajectory with two reflections in Fig. 3(b) contributes to the third "finger" in the bottom-right of the distribution.

The entry angle $\angle(v_y, v_x)$ of the parallel streaming electrons is similar to $\angle(B_y, B_x)$ at the entry position. This entry angle and the $v_x B_z$ magnetic forces, which rotate the velocity into the y-direction, control the angle between the striations of f in the v_x-v_y plane and vary discretely with the number of reflections. From here, it can be seen how the inflow anisotropy drives the current, as the large parallel streaming velocity of the electrons upstream of the layer gets turned

into the y-direction by the entry angle and by the magnetic forces. The narrow "tip" of the distribution with high number of reflections is due to the longer time this limited class of electrons is accelerated by E_y.

In addition, the structure of the distribution accounts for the momentum balance in the direction of the reconnection electric field. Close to the x-line, B vanishes and the off-diagonal terms of the pressure tensor are dominant, balancing the electric field

$$E_y \simeq -\frac{1}{ne}(\nabla \cdot \mathbf{P})_y = -\frac{1}{ne}\left(\frac{\partial P_{xy}}{\partial x} + \frac{\partial P_{yz}}{\partial z}\right), \quad (4)$$

where the frozen in condition $\mathbf{E} + \mathbf{v} \times \mathbf{B} = 0$ is broken by electron meandering motion.[23] These terms arise from the small changes in the distribution function between different positions. In Figs. 4(a), 4(b), 4(g), 4(h) (and Fig. 2(a)), moving from below to above x-line, the $v_z < 0$ portion of the distribution being slightly displaced in the negative v_y direction relative to the $v_z > 0$ portion and ends slightly displaced in the positive v_y direction, giving rise to a gradient in P_{yz}. The displacements are due to the different times electrons spend in the diffusion region, which affects the change in v_y due to acceleration by the reconnection electric field. The gradient in the P_{xy} term arises from the rotation of the distribution in the v_x-v_y plane as one moves along x, which is shown in Figs. 4(c) and 4(d).

A. Role of E_y and $\Phi_\parallel$ in determining the structure of f

The role of E_y in the acceleration of electrons in the narrow tip of the triangular distributions can be shown numerically. A series of simulations with parameters described in Ref. 9 were performed, with an additional force applied to electrons in a $40d_e \times 3d_e$ box around the x-line. In one simulation, this external force canceled the E_y component of the Lorentz force, while in another, the additional force doubled E_y. At all times were Maxwell's equations solved self-consistently. The electron distributions at the x-line from these simulations are shown in Fig. 5(a), and the dependence of the length of the tip on E_y is clear. In all cases, there is still turning of the electron velocity in the y direction due to the effects of the magnetic field.

The impact of using the anisotropic distribution, in particular, the large $\Phi_\parallel$, as a boundary condition is illustrated in Fig. 5(b), in which a reconstructed distribution function with $\Phi_\parallel = 0$ assumed in the inflow is compared to the distribution with the actual $\Phi_\parallel$ from the simulation. Without the large $\Phi_\parallel$ which gives rise to the elongated inflow distribution, the full length of the fingers in the reconstructed distribution is not observed.

IV. RECONNECTION WITH SMALL GUIDE FIELDS

In nature, the generic reconnection scenario includes a guide field, and its addition to the antiparallel reconnection geometry influences the structure of the reconnection region.[14,24] While at mass ratio 400, the electron jets mentioned in Sec. I are observed up to guide fields of $B_g = 0.14B_0$, recent full mass ratio simulations have shown that they no longer exist even for extremely small guide

fields $(B_g \gtrsim 0.05B_0)$.[14] The effects of small guide fields on spacecraft observations of reconnection will thus play an important role, and it is necessary to understand how the structure of the diffusion region changes with B_g.

In this section, results from mass ratio 400 simulations are first presented to illustrate the changes in the distribution function as the guide field is gradually increased from $0.05B_0$ to $0.2B_0$. The results of full mass ratio simulations, where the dependency on B_g is stronger, will then be shown.

A. Mass ratio 400 simulations

The simulations used have the same parameters as described in Sec. III, with the value of B_g being the only variable changed between simulations. Again, the orbit tracing method is applied to fields from time slices after reconnection has become steady state, and the form of the distribution function is thereby obtained. In Fig. 6, plots of E_z and the in plane electron flow U_{ex} in simulations with different values of B_g are shown. The two columns show the existence of the elongated region for guide fields up to $B_g = 0.14B_0$, and the disappearance of the jets at $B_g = 0.2B_0$.

A comparison between the x-line distributions for $B_g = 0$ and $B_g = 0.05B_0$ is shown in the first two columns of Fig. 7, revealing clear differences between their structures. In the top panels (v_y-v_z plane), the phase space hole in v_z closes when B_g is finite, and f is large around a region with small v_z, v_x, and negative v_y. Protruding from this central region are a number of "fingers" with different inclinations, which are most easily seen in the v_x-v_z plane.

The lack of a phase space hole in v_z is most easily explained and is due to the lack of the inversion layer of the
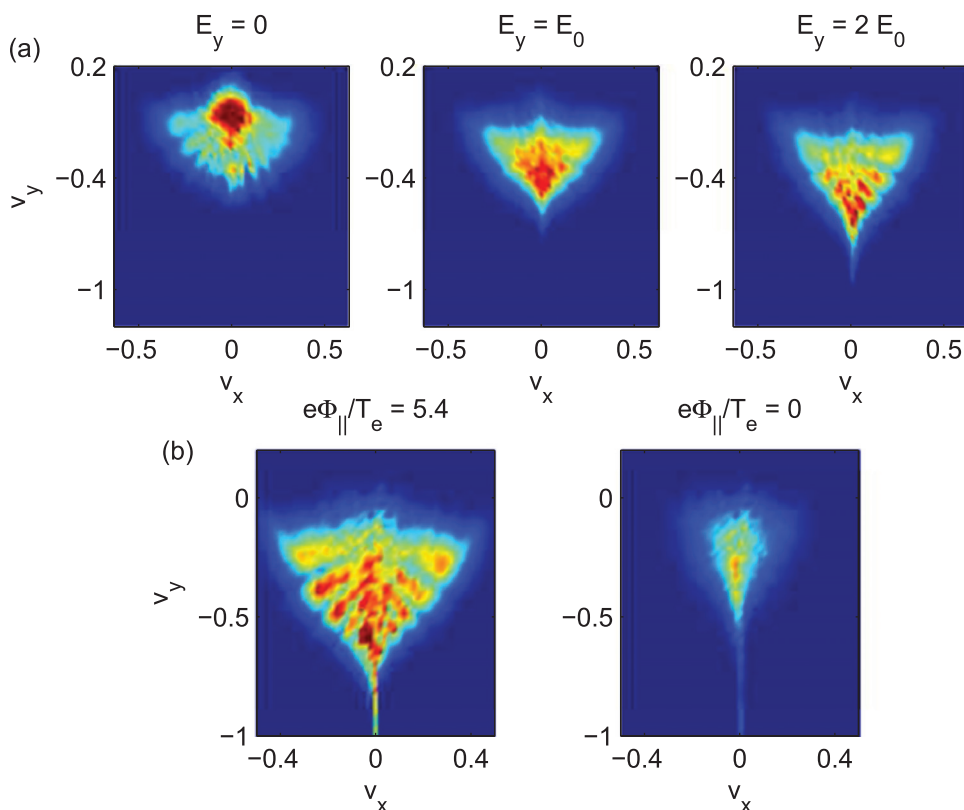

FIG. 5. (a) Electron distributions averaged over v_z at the x-line from simulations in which the force of E_y on the electrons is modified. In the left plot, there is no elongation due to the absence of E_y. The center plot shows the distribution in the unmodified simulation, while there is increased electron acceleration in the final plot, where E_y has been effectively doubled. (b) Comparison of the reconstructed distribution using $e\Phi_\parallel/T_e = 5.4$ (from simulation data) and 0 (assuming only magnetic trapping). The importance of the parallel potential in determining the length of the fingers is evident. Note that the data in (a) and (b) come from two different sets of simulations.
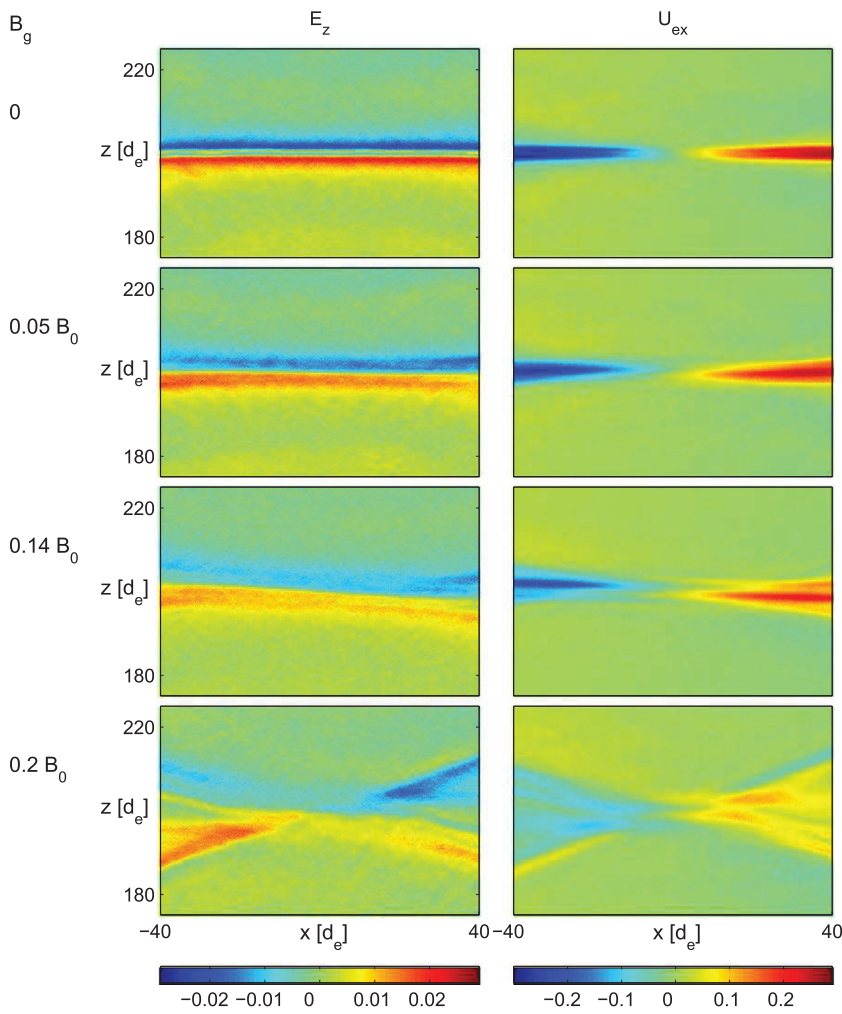
FIG. 6. Changes in the reconnection geometry as the guide field is increased from 0 to $0.2B_0$. The left column shows the in-plane electric field E_z, while the right column shows the electron flow velocity U_{ex} (in this figure, the x-axis is shifted such that the x-line is located at $(x, z) \simeq (0, 200)$). The electron Alfvén speed is 0.3c, so electrons in the jets are moving at this velocity.
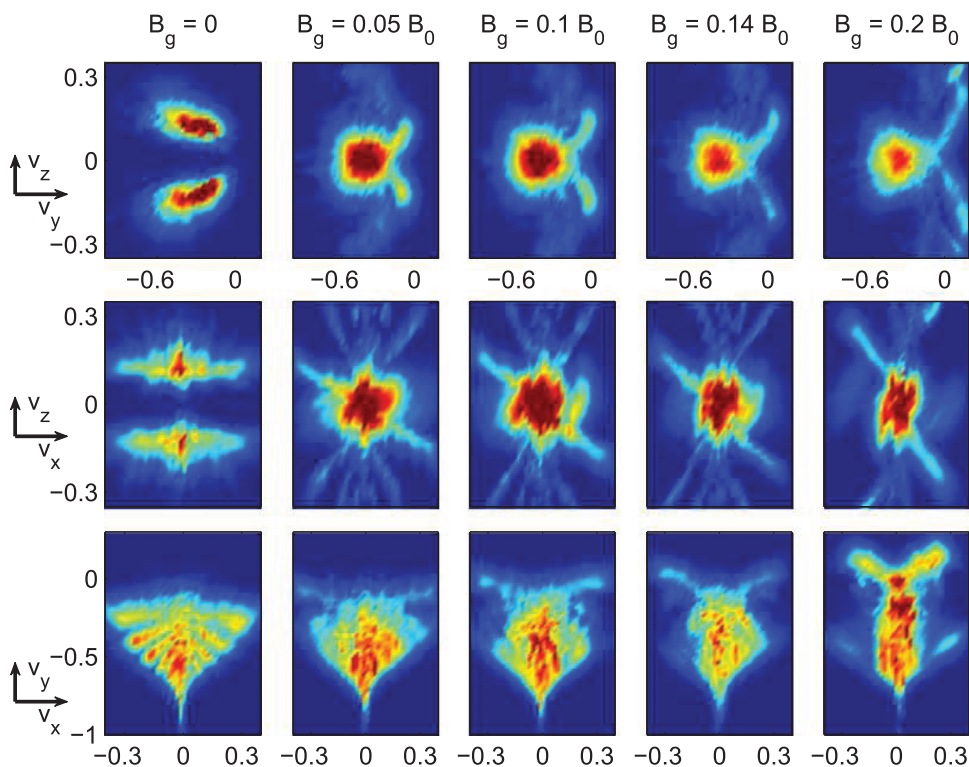

FIG. 7. Electron distributions at the x-line from simulations of reconnection with increasing guide fields. From left to right, $B_g = 0$, $0.05B_0$, $0.1B_0$, $0.14B_0$, and $0.2B_0$. At the largest guide field, the elongated electron jet is no longer present and the field geometry is different.

in plane electric field E_z in the diffusion region,[18] which allows electrons to reach the x-line without being accelerated in the z-direction. In order to understand the other features of the distribution, it is once again useful to trace the origin of the particles from different regions of velocity space, and count the number of times they cross $z = 200d_e$. This is illustrated in the three dimensional plots of the distribution and some characteristic orbits shown in Figs. 8 and 9.

The electrons in regions with large f correspond to two types of trajectories. In the central region of the velocity distribution, orbits are similar to those shown in Fig. 8(b), coming from the top right and bottom left quadrants in the inflow, where the guide field is in the same direction as the quadrupolar Hall field. Within the fingers, the orbits are like those in Fig. 8(c), coming from the regions where the guide field is in the opposite direction to the quadrupole field. On entering the layer, the particles exhibit oscillatory z motion with a large amplitude as they are ejected in the x direction.

The nature of these orbits also explains the alternation of the sign of v_z with the number of reflections for electrons with the same v_x sign. As the electrons in the fingers come from a lower B region with a thinner distribution (in the $v_\perp$ direction), the fingers are thinner than the central region. This behavior is unlike the antiparallel case, where all particles undergo similar types of motion.

The motion of electrons in the central area is well approximated by the model of Goldman *et al.*,[14] in which the equations of motion Eq. (3) are modified by the addition of the guide field and the replacement of v_y with the mean y fluid velocity. Setting $e/m_e = 1$ for convenience,

$$\ddot{x} = -U_y B_0 \frac{x}{L} + \dot{z} B_y, \quad \ddot{z} = U_y B_0 \frac{z}{d} - \dot{x} B_y. \tag{5}$$

The resulting linear equations of motion then account for vertical deflection of the trajectories as the electrons are ejected from the layer.
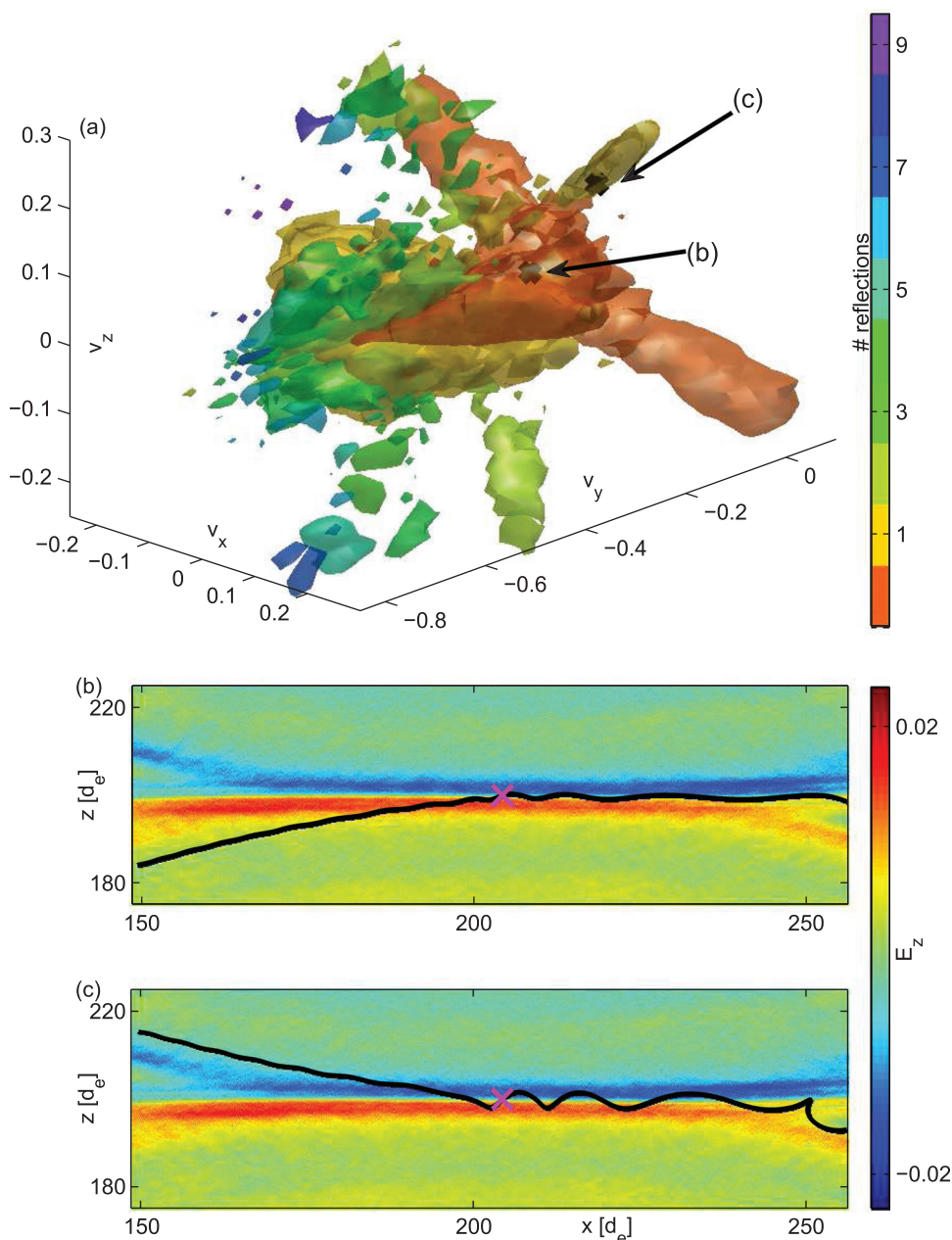

FIG. 8. (a) Isosurfaces of the electron distribution at the x-line for $B_g = 0.05B_0$. Colors show the number of times an electron is reflected before reaching the x-line. (b) Trajectory of an electron reaching the point marked (b) in velocity space from the left and exiting from the right. Likewise for (c).
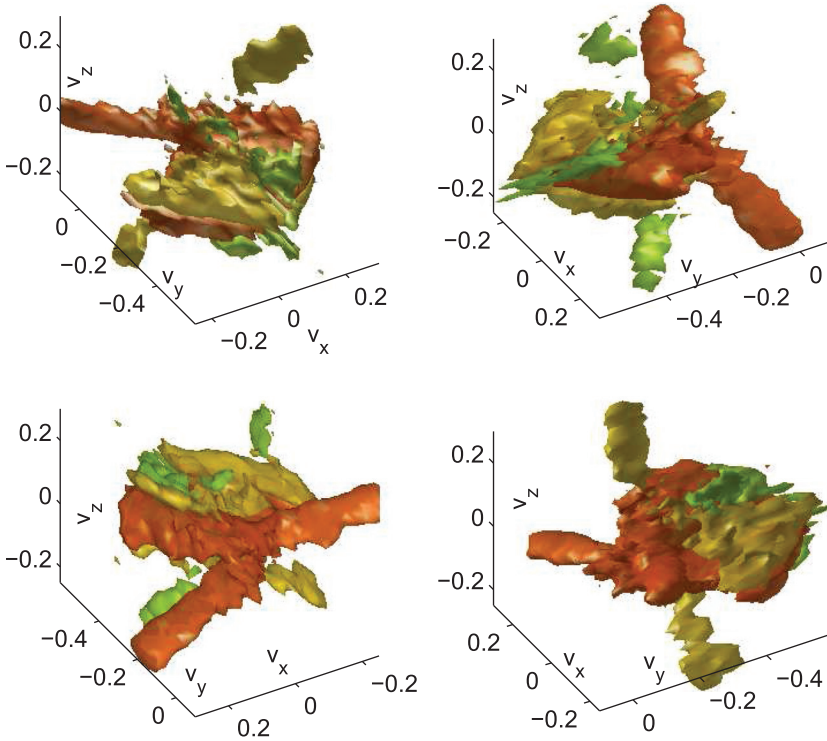
FIG. 9. Four different views of isosurfaces of the electron distribution at the x-line for $B_g = 0.05B_0$. Colors show the number of times an electron is reflected before reaching the x-line, and only regions with electrons with 0, 1, and 2 reflections are shown.

As seen in Figs. 7 and 8(a), the fingers in the distribution are inclined in both the v_x-v_y and v_x-v_z planes. The inclination in the v_x-v_y plane of the fingers with no reflections is due to the field-aligned motion in the inflow—the addition of the guide field means that the direction of the magnetic field just outside the layer is no longer purely in the x direction as in the antiparallel case. As in the antiparallel case, the large $\Phi_\parallel$ outside the layer determines the length of the fingers. The presence of the guide field ($B_y > 0$ near the x-line) also causes acceleration in the z direction due to the v_xB_y force, which accounts for the initial inclination in the v_x-v_z plane.

As the number of reflections increases, the angle of inclination (measured from the v_x axis) increases and the mean $|v_y|$ increases. Once again, the increase in $|v_y|$ is due to the turning effect of the magnetic field, with some contribution from E_y. The decrease in $|v_x|$ also follows from Eq. (5). The v_zB_y term is small when averaged over an oscillation period, so particles travelling towards the x-line are decelerated in a similar manner to the antiparallel case. However, a complete explanation of the acceleration in z requires the use of the full equation of motion and must be solved numerically.

Figure 10 provides an illustration of how the fingers from different positions in the diffusion region are related. In Figs. 10(a) and 10(b), distributions from the x-line and a point $5d_e$ to its left are displayed. The three colored points in each figure correspond to electrons following the trajectories in Fig. 10(c), and the point at which the distribution in (a) is evaluated is the average position of where the three trajectories first cross $z = 200d_e$. As the electrons move from (a), where they lie in the finger with no reflections, to (b), their positions in velocity space evolve until they eventually reside in the finger with one reflection in the distribution at the x-line. These numerical results thus demonstrate how the fingers in the distribution are related to one another.

The changes in the distribution as the guide field is increased are displayed in Fig. 7. The structure of the central region remains the same, and the changes are mostly seen in the fingers. Most evidently, in the v_x-v_y plane, they increase in inclination as B_g increases, due to the orientation of the external magnetic field as mentioned earlier. The difference between the $B_g = 0.2B_0$ case and the other distributions is due to the different field geometry, as the elongated electron layer is no longer present. Nevertheless, the general structure of the distribution at the x-line is similar. Thus, as B_g increases with the field geometry remaining similar, the effects on the distribution are small.

B. Mass ratio 1836 simulations

In the full mass ratio simulations, the size of the simulation domain in terms of d_i is maintained, and is 5120×5120 cells $= 857d_e \times 857d_e$. All other parameters remain as described in Sec. III. In agreement with Ref. 14, the electron jets are not present at the guide field $B_g = 0.05B_0$, though there is a somewhat elongated diffusion region.

Reconstructed distribution functions from the full mass ratio simulations are presented in Fig. 11. In the antiparallel case, the distribution has the same structure as in the antiparallel mass ratio 400 simulation shown in Fig. 3. This is expected as the field geometries and inflow distributions are similar.

However, at full mass ratio, the dependency on B_g is stronger than in the case with $m_i/m_e = 400$. At $B_g = 0.05B_0$, there is still an elongated region but electron jets are not present, indicating this value of B_g is close to the transition between reconnection with and without the electron jets. The distribution obtained has similarities to both the $B_g = 0.14B_0$ and $0.2B_0$ distributions at mass ratio 400.

As B_g is increased to $0.1B_0$, where there are no jets but the exhaust is unmagnetized, the distribution becomes more
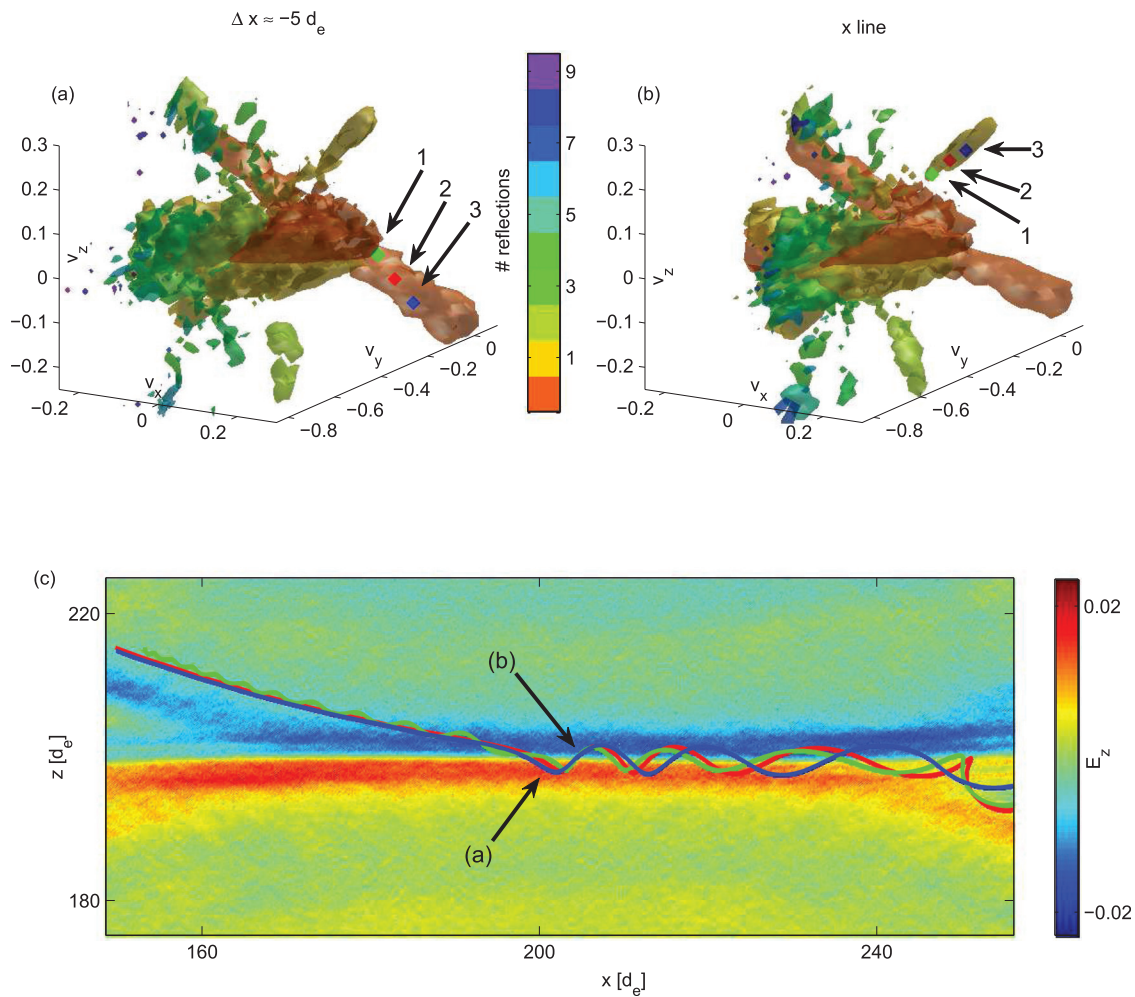
FIG. 10. A demonstration of the evolution of the velocity space positions of electrons in the fingers. Electrons from the zero-reflection finger in (a) follow the trajectories in (c) until they reach the one-reflection finger at the x-line (b). The distribution in (a) is taken from the average x position of the $z = 200d_e$ crossings of the three trajectories.
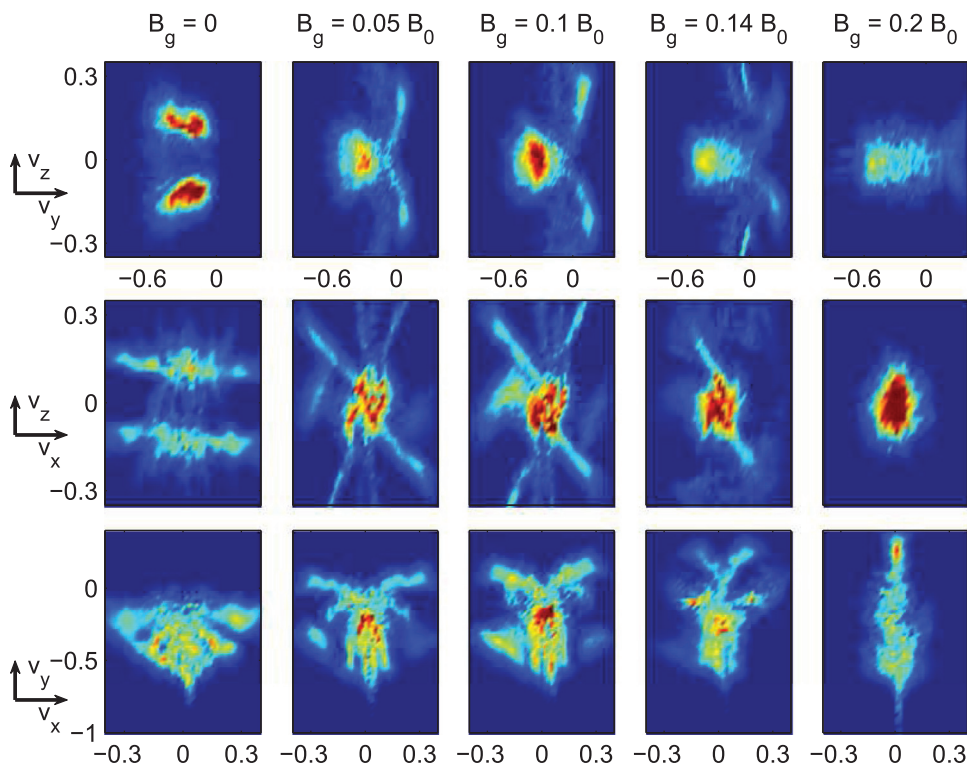

FIG. 11. Electron distributions at the x-line from full mass ratio simulations. From left to right, the $B_g = 0$ (antiparallel), $0.05B_0$, $0.1B_0$, $0.14B_0$, and $0.2B_0$. The antiparallel distribution has the same structure as in the mass ratio 400 antiparallel simulation, while the $B_g \neq 0$ cases are similar to larger guide field simulations at mass ratio 400.

similar to the $B_g = 0.2B_0$ case in the mass ratio 400 simulation. Above $B_g = 0.14B_0$ in the full mass ratio simulations, there is a transition to a geometry with a magnetized exhaust, and the distributions approach the anisotropic f given by Eq. (A2).

The correspondence of the distributions in simulations with stronger guide fields at low mass ratio and weaker guide fields at high mass ratio can be explained by considering the geometry of the magnetic fields. With the addition of a guide field, Eq. (1) becomes

$$\mathbf{B} = B_0\left(\frac{z}{d}\hat{\mathbf{x}} + \frac{x}{L}\hat{\mathbf{z}}\right) + B_g\hat{\mathbf{y}}. \tag{6}$$

In the simulations used above, the global field geometry depends on the ion inertial scale, so $d, L \propto d_i$, while the size of the electron scale current layers are governed by the electron skin depth, d_e. As such, the magnetic field can be written as

$$\mathbf{B} = B_0\left(\frac{z}{d_i\Delta}\hat{\mathbf{x}} + \frac{x}{d_i\Lambda}\hat{\mathbf{z}}\right) + B_g\hat{\mathbf{y}} = B_0\sqrt{\frac{m_e}{m_i}}\left(\frac{\tilde{z}}{\Delta}\hat{\mathbf{x}} + \frac{\tilde{x}}{\Lambda}\hat{\mathbf{z}}\right) + B_g\hat{\mathbf{y}}, \tag{7}$$

where $d = d_i\Delta$, $L = d_i\Lambda$, $\tilde{x} = x/d_e$, and $\tilde{z} = z/d_e$ and the relation $d_i = \sqrt{m_i/m_e}d_e$ has been used. The effect of the guide field on motion of electrons in simulations with constant $B_g^2 m_i/m_e$ is thus similar, which gives the observed relationship between the distributions at different mass ratios.

The results of these simulations have shown that the addition of a small guide field at realistic mass ratios leads to a dramatic modification of the reconnection geometry and the distribution function. As reconnection in the magnetotail takes place with guide fields in different regimes,[8,25,26] these results are relevant to NASA's upcoming MMS mission,[27] which will be able to resolve the electron diffusion region and electron distributions. The results also emphasize the importance of the mass ratio in the interpretation of results of simulations of reconnection with small guide fields.

V. SUMMARY AND CONCLUSION

The electron diffusion region in collisionless reconnection has been studied using orbit tracing techniques on data from kinetic simulations of magnetic reconnection. This technique allows the electron distribution $f(\mathbf{x}, \mathbf{v})$ to be evaluated at high resolution. In antiparallel reconnection, it has been shown that the strong inflow electron pressure anisotropy is responsible for the highly structured nature of the electron distribution in this region, and the origin of the off-diagonal terms of the pressure tensor has been revealed.

In the case of reconnection with a small guide field, the structure of the distribution is different from the antiparallel case, and these differences can be explained by considering the motion of single particles in the fields. It has also been shown that the reconnection geometry is sensitive to the mass ratio when guide fields are present, and this raises questions about the applicability of the results of low mass ratio simulations to spacecraft data with similar guide fields.

These results will be particularly relevant to the upcoming MMS mission. The spacecraft will have particle detectors with extremely high time resolution, allowing them to resolve the three dimensional structure of the electron distribution in the diffusion region studied here.

APPENDIX: MODEL FOR ELECTRON ANISOTROPY

The results of this paper make use of a recently derived model for the electron pressure anisotropy in guide field reconnection and the inflow region in antiparallel reconnection.[10] Assuming the electron thermal speed is much larger than the Alfvén speed $v_{the} \gg v_A$ and the adiabatic invariance of the magnetic moment $\mu = mv_\perp^2/2B$, an expression for the distribution function can be determined.

Far upstream of reconnection regions in the ambient plasma, the distribution function f_∞ of the electrons is assumed to be an isotropic Maxwellian. Because of the conservation of the magnetic moment μ, the perpendicular velocity of electrons approaching the diffusion region decreases as B decreases. At the same time, electrons moving along a field line gain energy due to acceleration by parallel electric fields, so that the total energy of an electron can be written as $\mathcal{E} = \mathcal{E}_\infty + e\Phi_\parallel$, where $\mathcal{E}_\infty$ is the initial energy and $\Phi_\parallel$ is an acceleration potential defined by

$$\Phi_\parallel(x) = \int_{\mathbf{x}}^{\infty} \mathbf{E} \cdot d\mathbf{l}, \tag{A1}$$

where the integration is carried out along the magnetic field lines. Here, it should be emphasized that $\Phi_\parallel$ is a pseudo potential characterizing the minimal energy required for an electron to escape the region in a straight shot along a field line. It should not be confused with the electrostatic potential, and can, in fact, take the opposite sign in certain regions.[10,28]

Using Liouville's theorem, which states that $df/dt = 0$ along particle trajectories, points in the reconnection region can be mapped to the ambient plasma, allowing the distribution to be determined by $f(\mathbf{x}, \mathbf{v}) = f_\infty(\mathcal{E}_\infty)$. It is important to note that particles can be divided into two categories—trapped particles which have almost no initial parallel velocity and drift into the region, and passing particles, which reach the region in a single shot along a field line.[10]

The distribution function thus takes the form

$$f(\mathbf{x}, \mathbf{v}) = \begin{cases} f_\infty(\sqrt{m_e^2c^4 + \wp^2c^2} - e\Phi_\parallel), & \text{passing} \\ f_\infty\left(\sqrt{\frac{B_\infty}{B}\wp_\perp^2 c^2 + m_e^2c^4}\right), & \text{trapped} \end{cases} \tag{A2}$$

where the energy at infinity is given by its relativistic form with $\wp^2 = \wp_\parallel^2 + \wp_\perp^2$, $\wp_\parallel = \gamma m_e v_\parallel$ and $\wp_\perp = \gamma m_e v_\perp$. Using this relativistic generalization of the form for f given in

Ref. 10 was necessary for obtaining the agreement between the moments of the reconstructed distributions and those directly taken from the PIC simulations (see Fig. 2).

As shown by Le *et al.*,[11] expressions of the density and parallel and perpendicular pressures as functions of $\Phi_\parallel$ and B are obtained by taking moments of the distribution function. By eliminating $\Phi_\parallel$, equations of state for the pressure $p_\parallel(n, B)$ and $p_\perp(n, B)$ can be found. The scalings $p_\parallel \propto n^3/B^2$ and $p_\perp \propto nB$ then explain the strong pressure anisotropy in regions of high density and small magnetic fields.

[1]J. Dungey, Philos. Mag. **44**, 725 (1953).

[2]J. B. Taylor, Rev. Mod. Phys. **58**, 741 (1986).

[3]V. M. Vasyliunas, Rev. Geophys. **13**, 303, doi:10.1029/RG013i001p00303 (1975).

[4]T. D. Phan, L. M. Kistler, B. Klecker, G. Haerendel, G. Paschmann, B. U. O. Sonnerup, W. Baumjohann, M. B. Bavassano-Cattaneo, C. W. Carlson, A. M. Dilellis, K. H. Fornacon, L. A. Frank, M. Fujimoto, E. Georgescu, S. Kokubun, E. Moebius, T. Mukai, M. Oieroset, W. R. Paterson, and H. Reme, Nature **404**, 848 (2000).

[5]S. Masuda, T. Kosugi, H. Hara, and Y. Ogawaray, Nature **371**, 495 (1994).

[6]J. Birn, J. F. Drake, M. A. Shay, B. N. Rogers, R. E. Denton, M. Hesse, M. Kuznetsova, Z. W. Ma, A. Bhattacharjee, A. Otto, and P. L. Pritchett, J. Geophys. Res. **106**, 3715, doi:10.1029/1999JA900449 (2001).

[7]M. Oieroset, R. Lin, and T. Phan, Phys. Rev. Lett. **89**, 195001 (2002).

[8]L. J. Chen, N. Bessho, B. Lefebvre, H. Vaith, A. Fazakerley, A. Bhattacharjee, P. A. Puhl-Quinn, A. Runov, Y. Khotyaintsev, A. Vaivads, E. Georgescu, and R. Torbert, J. Geophys. Res. **113**, A12213, doi:10.1029/2008JA013385 (2008).

[9]J. Ng, J. Egedal, A. Le, W. Daughton, and L.-J. Chen, Phys. Rev. Lett. **106**, 065002 (2011).

[10]J. Egedal, W. Fox, N. Katz, M. Porkolab, M. Oieroset, R. P. Lin, W. Daughton, and J. F. Drake, J. Geophys. Res. **113**, A12207, doi:10.1029/2008JA013520 (2008).

[11]A. Le, J. Egedal, W. Daughton, W. Fox, and N. Katz, Phys. Rev. Lett. **102**, 085001 (2009).

[12]W. Daughton, J. Scudder, and H. Karimabadi, Phys. Plasmas **13**, 072101 (2006).

[13]A. Le, J. Egedal, W. Fox, N. Katz, A. Vrublevskis, W. Daughton, and J. F. Drake, in 51st Annual Meeting of the Division of Plasma Physics of the American Physical Society, Atlanta, GA, 02–06 November 2009 [Phys. Plasmas **17**, 055703 (2010)].

[14]M. V. Goldman, G. Lapenta, D. L. Newman, S. Markidis, and H. Che, Phys. Rev. Lett. **107**, 135001 (2011).

[15]K. J. Bowers, B. J. Albright, L. Yin, B. Bergen, and T. J. T. Kwan, Phys. Plasmas **15**, 055703 (2008).

[16]E. Harris, Il Nuovo Cimento **23**, 115 (1962).

[17]R. Horiuchi and H. Ohtani, Commun. Comput. Phys **4**, 496 (2008).

[18]L.-J. Chen, W. S. Daughton, B. Lefebvre, and R. B. Torbert, Phys. Plasmas **18**, 012904 (2011).

[19]T. Speiser, Planet. Space Sci. **18**, 613 (1970).

[20]E. Priest and T. Forbes, *Magnetic Reconnection* (Cambridge University Press, 2000).

[21]A. Divin, S. Markidis, G. Lapenta, V. S. Semenov, N. V. Erkaev, and H. K. Biernat, Phys. Plasmas **17**, 122102 (2010).

[22]K. Fujimoto and R. D. Sydora, Phys. Plasmas **16**, 112309 (2009).

[23]A. Ishizawa, R. Horiuchi, and H. Ohtani, Phys. Plasmas **11**, 3579 (2004).

[24]M. Swisdak, J. F. Drake, M. A. Shay, and J. G. McIlhargey, J. Geophys. Res. **110**, A05210, doi:10.1029/2004JA010748 (2005).

[25]M. Oieroset, T. Phan, M. Fujimoto, R. P. Lin, and R. P. Lepping, Nature **412**, 414 (2001).

[26]T. D. Phan, J. F. Drake, M. A. Shay, F. S. Mozer, and J. P. Eastwood, Phys. Rev. Lett. **99**, 255002 (2007).

[27]A. S. Sharma and S. A. Curtis, *Nonequilibrium Phenomena in Plasmas*, Astrophysics and Space Science Library Vol. 321, edited by W. Burton, J. M. E. Kuijpers, E. P. J. Heuvel, H. Laan, I. Appenzeller, J. N. Bahcall, F. Bertola, J. P. Cassinelli, C. J. Cesarsky, O. Engvold, R. McCray, P. G. Murdin, F. Pacini, V. Radhakrishnan, K. Sato, F. H. Shu, B. V. Somov, R. A. Sunyaev, Y. Tanaka, S. Tremaine, N. O. Weiss, A. S. Sharma, and P. K. Kaw (Springer, Netherlands, 2005), pp. 179–195.

[28]J. Egedal, W. Daughton, J. F. Drake, N. Katz, and A. Le, Phys. Plasmas **16**, 050701 (2009).